Anisotropic Acoustic Plasmons in Black Phosphorus

In-Ho Lee, Luis Martín-Moreno, Daniel A Mohr, Kaveh Khaliji, Tony Low, and Sang-Hyun Oh

ACS Photonics, **Just Accepted Manuscript** • Publication Date (Web): 11 Mar 2018

Anisotropic Acoustic Plasmons in Black Phosphorus

In-Ho Lee,[1] Luis Martin-Moreno,[2,*] Daniel A. Mohr,[1] Kaveh Khaliji,[1]

Tony Low,[1,*] and Sang-Hyun Oh[1,*]

[1] Department of Electrical and Computer Engineering, University of Minnesota, Minneapolis, Minnesota, 55455, U.S.A.

[2] Instituto de Ciencia de Materiales de Aragón and Departamento de Física de la Materia Condensada, CSIC-Universidad de Zaragoza, E-50009 Zaragoza, Spain.

*E-mail: lmm@unizar.es (L.M.-M.), tlow@umn.edu (T.L.), sang@umn.edu (S.-H.O.)

ABSTRACT

Graphene separated a few nanometers away from a metal surface can support 'acoustic plasmons', which exhibit extreme plasmon confinement an order of magnitude higher than that of conventional graphene plasmons. Here, we investigate acoustic plasmons supported in a monolayer and multilayers of black phosphorus (BP) placed shortly above a conducting plate. In the presence of a conducting plate, the acoustic plasmon dispersion for the armchair direction is found to exhibit the characteristic linear scaling in the mid- and far-infrared regime while it largely deviates from that in the long-wavelength limit and near-infrared regime. For the zigzag direction, such scaling behavior is not evident due to relatively tighter plasmon confinement. Further, we demonstrate a new design for an acoustic plasmon resonator that exhibits higher plasmon confinement and resonance efficiency than BP ribbon resonators in the mid-infrared and longer wavelength regime. Theoretical framework and new resonator design studied here provide a practical route toward the experimental verification of the acoustic plasmons in BP and open up the possibility to develop novel plasmonic and optoelectronic devices that can leverage its strong in-plane anisotropy and thickness-dependent band gap.

KEYWORDS. black phosphorus, acoustic plasmon, gap plasmon, surface plasmon polaritons, anisotropy, two-dimensional material.

Two dimensional (2D) materials[1,2] have attracted enormous interest due to their unique properties such as ultrahigh charge carrier mobility,[3,4] anomalous quantum Hall effect,[5] and strong light-matter interaction.[6,7] Among a variety of such exciting properties, strong light-matter interactions in 2D materials are particularly intriguing considering the extreme size mismatch between their atomic-scale thicknesses and wavelengths of free-space light, λ_0. Moreover, this feature plays a central role in many potential applications of 2D materials such as optical modulators,[8,9] metasurfaces,[10-13] biosensors,[14,15] and photodetectors.[16,17] For a particular set of 2D materials including graphene, light-matter interactions can be even more intense because of the excitation of surface plasmons.[18-20] Compared to conventional surface plasmons in noble metals, the plasmons in 2D materials exhibit tighter confinement ($\sim\lambda_0/100$)[21-23] as well as tunability by extrinsic doping.[20,24] Many researchers have demonstrated that such features allow for the development of nanoscale photonic and optoelectronic devices that have novel functionality and superior performance inaccessible with conventional materials.[15,25,26]

Recent work on graphene indicates that the plasmon wavelength, and accordingly the confinement of 2D plasmons, can be further reduced in the presence of a conducting plate adjacent to the graphene.[27-30] As in the case of spatially separated double-layer graphene,[31,32] the hybridization of two plasmons in a graphene sheet and its mirror image leads to the formation of two plasmon branches: less confined 'optical' and highly confined 'acoustic' plasmons, depending on whether charges in two layers oscillate in-phase or out-of-phase. In the double-layer case with a gap much smaller than plasmon wavelength, the acoustic mode with out-of-phase charge oscillation becomes a dark mode due to the cancellation between dipole momenta in two layers, while the optical mode that has a net dipole momentum is optically active.[33] In the present case of a 2D layer on metal, however, the acoustic mode becomes optically active in the

absence of a second 2D layer to cancel the dipole momentum, while the optical mode is prohibited since it mandates the tangential electric fields to be non-zero at the surface of the conducting plate. Due to the out-of-phase charge oscillations, the vertical electric fields of acoustic plasmons are largely confined within the nanometric gap with a conducting plate, which gives extreme plasmon confinement defined by the gap size. In contrast to conventional graphene plasmons or a 2D electron gas that has a parabolic dispersion, interestingly, acoustic plasmons exhibit a linear dispersion at small frequencies.[28-30]

Recently, black phosphorus (BP) has been extensively studied as a novel anisotropic plasmonic material.[34-39] In contrast to other 2D plasmonic materials, the inherent in-plane anisotropy of BP renders the plasmon dispersion dependent on the propagation direction.[34] These anisotropic plasmons are expected to enable the development of novel polarization-dependent optoelectronic devices such as optical modulators,[40,41] tunable polarization rotators,[37,42] and polarization-sensitive photodetectors.[43,44] One possible way to maximize the light-matter interaction in BP for such applications is to leverage the extreme confinement of acoustic plasmons. In this regard, it is imperative to understand how the in-plane anisotropy of BP is manifested through the acoustic plasmon dispersion and how these plasmons enhance the light-matter interactions in BP. For practical applications, in addition, new resonator configurations for acoustic plasmons that require minimal post-processing after the BP deposition should be investigated due to its instability in the ambient environment.[45,46]

In this work, we theoretically investigate the dispersion of acoustic plasmons in freestanding BP placed adjacent to a conducting plate. Using both analytical and numerical approaches, we study how the in-plane anisotropy of BP is reflected in the plasmon dispersion and how the acoustic plasmons scale with frequency ω and gap size g with a conducting plate. The effect of

doping and BP thickness is examined as well. Further, we propose a practically viable and highly efficient design for an acoustic plasmon resonator, for which we use a modified Fabry-Perot (F-P) resonance model to describe the resonant behavior.

RESULTS AND DISCUSSION

Theory. In the geometrical configuration considered here, a BP layer is placed above a conducting plate, and the distance between them is denoted by g (see Figure 1a). We consider surface plasmons propagating in the positive x direction. In order to study the influence of BP anisotropy on plasmon propagation, one of the two principal lattice axes, i.e., 'armchair' (AC) and 'zigzag' (ZZ), is aligned along the x direction. Figure 1b shows typical electric field distributions of conventional BP surface plasmons propagating along the AC direction for λ_0 = 25 μm for comparison. Here, we used five layers of BP (thickness t = 2.675 nm) and assumed a damping constant of η = 10 meV and an electron density of $n = 1\times10^{13}$ cm^{-2}. Although no reliable experimental values for the damping constant have been reported so far, previous research on graphene, which has similar damping pathways, indicates that a damping constant of 10 meV is within an experimentally feasible range,[20] and accordingly, this value has been widely used in BP studies.[34,37] From now on, we will use the same condition for BP unless mentioned otherwise. The conductivities we used for numerical simulations are summarized in the supplementary material. Throughout the paper, we will mostly focus on the case of five layers due to their experimental feasibility and reproducibility.[47] However, we will still investigate the cases with a different number of layers including a monolayer for completeness. Conventional BP plasmons exhibit a symmetric field profile with the plasmon wavelength λ_c = 1200 nm, which gives the vertical confinement of $\lambda_c/2\pi$ = 191 nm. Figures 1c and 1d show the field distributions

in the presence of a conducting plate for g = 5 nm and λ_0 = 25 μm. As in the case of graphene,[28-30] the electric field is constant across the gap region due to the out-of-phase charge oscillation between the BP layer and the conducting plate, which clearly shows that the observed mode is an acoustic plasmon. For the given λ_0, the vertical confinement of the acoustic plasmon within the gap is λ_0/5,000, which is around 38 times higher as compared to conventional plasmons propagating in the AC direction and 3 times higher than that of plasmons propagating in the ZZ direction. Contrary to the graphene case, the acoustic plasmon wavelength λ_{ac} largely differs for the two orthogonal directions (260 nm and 56 nm for AC and ZZ direction), which implicates a strong in-plane anisotropy in the plasmon dispersion for the BP case.

Before numerical investigation, we derive an analytical expression for the plasmon dispersion. The details for the mathematical derivation can be found in the supplementary material. Here, we define the dimensionless momentum q as k/k_0 with the plasmon wavenumber in the x direction k and the free-space wavenumber $k_0 \equiv \omega/c$, with c being the speed of light in free-space. Thus, Re(q) directly gives the ratio of λ_0/λ_{ac}. For Re(q)$\hat{g} \ll 1$, the plasmon dispersion for a BP layer on a freestanding plane in a vacuum is given as follows.

$$q = \frac{i}{4\alpha} + \sqrt{\left(\frac{i}{4\alpha}\right)^2 + \frac{i}{2\alpha\hat{g}}}, \tag{1}$$

with the dimensionless conductivity $\alpha \equiv (2\pi\sigma)/c$ and the dimensionless gap height $\hat{g} \equiv k_0 g$. The in-plane anisotropy of BP is accounted for by using the anisotropic conductivity σ (in Gaussian units).[34]

$$\sigma = \sigma_{AC}\cos^2\theta + \sigma_{ZZ}\sin^2\theta. \tag{2}$$

Here θ is the angle of propagation direction with the AC axis. We show that at low frequencies satisfying $\omega \ll 4\sqrt{D/g}$ with the anisotropic Drude weight $D = D_{AC}\cos^2\theta + D_{ZZ}\sin^2\theta$, the plasmon dispersion in Eq. (1) is further simplified to

$$q = \frac{1}{\sqrt{-2i\alpha\hat{g}}}. \tag{3}$$

Under the additional assumption of $\eta/\hbar \ll \omega$, Eq. (3) becomes $c/\sqrt{4gD}$ so that q becomes constant in ω and scales with g as $g^{-1/2}$. Thus, the plasmon dispersion in Eq. (3) clearly shows the characteristic features of acoustic plasmons. Note that the constant q in ω represents linear scaling with ω in terms of k since $k = q\omega/c$. The linear scaling regime is accordingly given by the intersection of three inequalities; (1) $\omega < 2\sqrt{D/t}$ ($\equiv \omega_{pl}$), (2) $\mathrm{Re}(q)\hat{g} \ll 1$, (3) $\eta/\hbar \ll \omega \ll 4\sqrt{D/g}$. The inequality (1) comes from the condition for the existence of plasmons, $\mathrm{Re}(\varepsilon_{BP}) < 0$, with the effective permittivity of BP, $\varepsilon_{BP} = 1+i(4\pi\sigma)/(\omega t)$, where the first (second) term denotes dielectric (Drude) response.[48] In the limit of zero thickness, the former is negligible, and its contribution increases with thickness. Similarly, a reduced doping will also enhance the relative dielectric contribution. Lastly, let us consider the two cases outside of linear scaling regime. At $0 \leq \omega \lesssim \eta/\hbar$, the plasmon dispersion in Eq. (3) scales with ω as $\omega^{-1/2}$ due to the increase in $\mathrm{Re}(\sigma)$. At high frequencies where $1 \lesssim \mathrm{Re}(q)\hat{g}$, on the other hand, the plasmon dispersion asymptotically approaches that of conventional plasmons without a conducting plate.

Acoustic Plasmon Dispersion. Plasmon dispersion curves for five layers of BP from numerical simulations along with those from Eq. (1) in the case of g = 5 nm are shown in Figure 2a. In addition, the plasmon dispersion for the case of conventional plasmons without a conducting plate is plotted alongside for comparison. As shown in the figure, generally, $\mathrm{Re}(q)$ for the AC direction is smaller at a given ω because of a larger σ. In the case of conventional

plasmons without a conducting plate, Re(q) for the AC direction follows the classical parabolic scaling behavior (which corresponds to linear scaling with ω in terms of q), while for the ZZ direction, it largely deviates from that. This is attributed to the fact that λ_c becomes comparable to t as ω approaches ω_{pl} = (0.175 eV)/$\hbar$. The AC case shows no such tendency since ω_{pl} corresponds to higher frequency, (0.593 eV)/$\hbar$. In the presence of a conducting plate, the plasmon dispersion for the AC direction is nearly constant in ω at most of frequencies showing the characteristic scaling behavior of acoustic plasmons except for the near-infrared (IR) regime and very small frequencies satisfying $0 \leq \omega \lesssim \eta/\hbar$. In the near-IR regime, λ_{ac} is comparable to g so that the plasmon dispersion follows the conventional case. For $0 \leq \omega \lesssim \eta/\hbar$, Re($q$) increases with decreasing ω as $\omega^{-1/2}$ as expected from Eq. (3), which is the same for the ZZ direction. Physically, such divergent behaviors come from overdamped oscillations, as the real part of conductivity becomes very large at such low frequencies. In contrast to the AC case, however, the plasmon dispersion for the ZZ direction shows no linear scaling behavior owing to larger Re(q) and smaller ω_{pl}. As $\omega \rightarrow$ (0.175 eV)/$\hbar$, it follows that for the case without a conducting plate. The larger Re(q) for the ZZ direction also results in a significant discrepancy between the numerical and the analytical results for the acoustic dispersion as well, while the two results for the AC direction are in a good agreement because of a smaller Re(q).

Figure 2b shows the figure of merit (FOM), Re(q)/Im(q), for the plasmon dispersions given in Figure 2a. At small frequencies, the FOM increases almost linearly with ω and the FOMs for different crystal axes have the similar value, as expected from the analytical results (see supplementary material). At higher frequencies, however, it starts to deviate from this trend before rolling down with increasing ω as intraband Landau damping sets in. Particularly for the ZZ direction, FOM becomes zero at ω = (0.175 eV)/$\hbar$. In contrast, the AC case is found to be

less damped and persists up to the near-IR regime due to lower plasmon confinement and larger ω_{pl} = (0.593 eV)/$\hbar$. The numerical results also agree with the analytical results in that the FOM for acoustic plasmons is always larger than those for conventional plasmons when Re(q)$\hat{g} \ll 1$. In Figures 2c and 2d, we examined the effect of g on Re(q) and FOM given ω = 0.025 eV. For a small g, where Re(q)$\hat{g} \ll 1$, Re(q) scales with g as $g^{-1/2}$ since it follows Eq. (1). For a large g, the analytical expression deviates from the numerical results and Re(q) asymptotically approaches the conventional case. Figure 2d shows the decrease in the FOM as the plasmon nature changes from acoustic to conventional.

Doping and Number of Layers Dependence. From a practical viewpoint, it is important to consider the effect of the electron density, n, as well as the number of layers, N, on the acoustic plasmon dispersion, since many potential applications require an active tuning of the optical properties of 2D materials. The plasmon dispersion at different n is shown in Figure 3a. With increasing n, Re(q) decreases at a fixed ω due to the increase in D and accordingly σ.[34] In addition, the increase in D broadens the plasmon-supporting band limited by ω_{pl}. In the ZZ case, in particular, ω_{pl} is located within the frequency range of interest leading to substantial change in the dispersion with n. In the AC case, ω_{pl} is in the near-IR regime so that the plasmon dispersion is less sensitive to n. For both directions, the FOM increases with increasing n at a given ω because of lower plasmon confinement (Figure 3b). At low frequencies, however, the FOM does not change appreciably with n.

Shown in Figure 3c is how the acoustic plasmon dispersion changes with increasing N for g = 5 nm. Here, we fixed n to be 1×10^{13} cm^{-2}. For larger N, more sub-bands contribute to the optical absorption, thereby increasing D.[34] For the AC direction, this leads to a slight decrease in Re(q) as N increases. The increase in Re(q) for N = 20 in the near-IR regime is attributed to the

decrease in ω_{pl}. The change in ω_{pl} leads to the significant changes in the plasmon dispersion for the ZZ direction as well. With decreasing N, the FOMs have a larger value for a broader frequency range (Figure 3d). Note that the results in Figure 3 indicate the larger asymmetry in the dispersion for small n and larger N, which agrees well with the expectation from the anisotropy in σ (Figure S1b).

Modal Reflection of Acoustic Plasmons. In addition to the plasmon dispersion, the modal reflection of plasmons plays an important role in predicting the behavior of plasmonic resonators.[49] In this regard, we investigated the reflectance and reflection phase picked up by acoustic plasmons at the open edge of a BP/free-space/conducting plate system. Here, we focus on two different types of edge termination; semi-infinite BP/semi-infinite conducting plate (SBSC) and infinite BP sheet/semi-infinite conducting plate (IBSC), which are schematically illustrated in Figures 4a and 4b. Figures 4c and 4d show the electric field distributions along the AC direction after reflection at the SBSC and IBSC edges. In the SBSC case, acoustic plasmons are almost totally reflected, while in the IBSC case, they are coupled to conventional BP plasmons in the metal-free region.

Figures 4e and 4f show the reflectance and reflection phase picked up by plasmons after reflection at the SBSC and IBSC edges for different g of 2, 5, and 10 nm. In the SBSC case, the reflectance of acoustic plasmons is always close to unity due to the absence of a waveguide mode in free-space, similar to the graphene ribbon case.[49] For the ZZ direction where λ_{ac} easily becomes comparable to t, the reflectance is smaller due to more efficient coupling to photonic radiation modes at the edge. In the long wavelength limit where acoustic plasmons are more confined within the gap, the reflection phase approaches that for the metal gap plasmon case, $-\pi$, due to the similarity in the mode profile.[50,51] With increasing ω, the reflection phase converges to

a value around -0.5π. For the ZZ direction, the reflection phase converges to this value more rapidly as $\omega \rightarrow (0.175\ \text{eV})/\hbar$. Note that the non-trivial reflection phase obtained here is somewhat different from that for the monolayer graphene case, -3/4π,[49] because of the larger thickness of five layers of BP. However, our numerical results show that -3/4π is recovered for a monolayer of BP.

In contrast to the SBSC case, the reflectance for the IBSC case abruptly decreases with increasing ω so that at high frequencies, the reflection becomes negligible (Figure 4f). This is because of the small difference in q between acoustic and conventional plasmons, which also accounts for the smaller reflectance for the cases of propagation in the ZZ direction and larger gaps. The reflection phase scales with ω similarly to the SBSC case, except that it has larger values at most frequencies and converges more rapidly. Note that we neglect the reflection phases for the ZZ direction at around $\omega = \omega_{\text{pl}}$, since the numerical simulations fails to give reliable values for the reflection phase because of a negligibly small λ_{ac}.

Optical Responses of Acoustic Plasmon Resonators. From our numerical results for the plasmon dispersion and the reflection phase, we estimate the resonant frequencies of two different types of acoustic plasmon resonators, having either periodic ribbons or a continuous BP sheet on a periodic array of conducting plates (gold). These two configurations are considered due to their experimental feasibility. The other feasible design, BP ribbons on a continuous conducting plate, is excluded due to its small far-field signal compared to the other configurations (see Figure S4). We also focus only on the AC case to compare the resonant behaviors of different configurations (for the ZZ direction, see supplementary material). Figure 5a shows the far-field extinction spectra for the case of BP(ribbon)/metal(ribbon) with g = 5 nm as a function of inverse conducting plate width (1/w). We set the distance between two

neighboring gold plates to be w as well. The far-field extinction is defined by 1-T with T being the far-field transmittance normalized to that without a resonator. The red dashed lines show the estimated resonant frequencies from the plasmon dispersion in Figure 2a and the reflection phase shown in Figure 4e using the F-P equation, which is

$$2k_{ac}w + 2\Phi_r = 2m\pi, \quad (4)$$

where k_{ac}, Φ_r and m represent the wavenumber of acoustic plasmons, the reflection phase at the edge and the order of the F-P resonance, respectively. As shown in the figure, the estimated resonant frequencies for different F-P resonance orders agree very well with full numerical results. Figure 5b shows extinction spectra for the case of BP(sheet)/metal(ribbon). In contrast to the previous case, the estimated resonant frequencies using the reflection phase in Figure 4f significantly deviates from full numerical results. In the BP(sheet)/metal(ribbon) case, the unit cell of the plasmon resonator should be considered as a combination of two F-P resonators formed within the gap and intermediate region. The modified F-P model gives the resonant condition as (see supplementary material for details),

$$2k_{ac}w + 2k_c w = 2l\pi. \quad (5)$$

Here, k_c represents the wavenumber of conventional plasmons, and l is the order of F-P resonances. As shown in the figure, the resonance frequency estimated from the new model is a decent match with numerical results. We emphasize that in the modified F-P model, the zeroth-order F-P resonance is not allowed due to the absence of the phase term in Eq. (5) and accordingly the first occurring mode corresponds to the second-order F-P resonance. As a result, the plasmon resonances can occur at higher frequencies than the case of BP(ribbon)/metal(ribbon).

Comparison of Resonator Designs. Based on the resonance model developed above, we investigate the extinction intensities of two different acoustic plasmon resonators together with a conventional BP ribbon resonator. Figures 6a-c illustrate optical coupling routes in three different designs. In the BP(ribbon) and BP(ribbon)/metal(ribbon) cases, incident waves are coupled to conventional surface plasmons or acoustic plasmons directly after scattering at the edge of resonator units. In the BP(sheet)/metal(ribbon) case, however, incident waves can launch both conventional and acoustic plasmons. Because of small reflection at the resonator edge, two plasmons are efficiently coupled to each other during propagation within the resonator, which can be considered as an indirect coupling of incident waves to plasmons. The electric field enhancement maps at the first occurring resonance (ω_R = 0.083 eV/$\hbar$) of three different designs are shown in Figures 6d-f. The BP(sheet)/metal(ribbon) case shows the largest field enhancement on resonance than those of the other configurations. Figures 6e and 6f clearly show that the resonances indeed result from the acoustic (out-of-phase) mode as can be seen from highly confined and vertically constant electric fields within the gap. In the double ribbon case where the charges in two layers oscillate in-phase, however, the electric fields inside the gap are appreciably weak confirming that the optical (in-phase) mode is an active mode (see supplementary materials).

Figure 6g shows the extinction spectra for three different configurations where the first-occurring resonances coincide at ω_R = (0.083 eV)/ $\hbar$. Among three designs, the BP(sheet)/metal(ribbon) design shows the largest extinction intensity on resonance while the BP(ribbon)/metal(ribbon) case exhibits the smallest intensity. In addition, the higher order modes of the BP(sheet)/metal(ribbon) resonator have larger extinction intensities than those of the BP(ribbon) resonator, which indicates that the background transmission in the

BP(sheet)/metal(ribbon) resonator remains relatively smaller for a given w. We found out that the trend in Figure 6g between three designs holds in mid-IR and longer wavelength regimes, which covers most of the frequency range of interest (Figure 6h). With the same BP material parameters, the BP(sheet)/metal(ribbon) case exhibits the largest extinction on the first-occurring resonance of up to 60% for $\omega_R < 0.142$ eV/$\hbar$. Using the plasmon dispersion and the extinction results in Figure 6h, we calculate the efficiency of coupling from free-space waves to plasmons, κ, for different designs as given in the inset (for the details, see supplementary material). The inset shows that for the BP(sheet)/metal(ribbon) resonator, the coupling from free-space waves to acoustic plasmons is several times more efficient than the BP(ribbon) case. The strong coupling efficiency for the BP(sheet)/metal(ribbon) case is attributed to the fact that the metal(ribbon) array is highly efficient in focusing the free-space light into a slit mode between the conducting plate units, which facilitates coupling to the plasmon mode. The presence of the metal(ribbon) array also helps to reduce the background transmission for a large w, which explains the larger extinction intensities for higher order modes compared to the BP(ribbon) case. The similarity in the scaling behavior of the coupling efficiency between the BP(ribbon) and the BP(sheet)/metal(ribbon) indicates that the focused light in the slit mode in the BP(sheet)/metal(ribbon) case mostly excites acoustic plasmons via conventional plasmons as suggested in Figure 6c. At higher frequencies, however, the extinction intensity for the BP(ribbon) case is larger due to the significant increase in the other contributor to extinction intensity, i.e., a cavity quality factor, which is determined by the propagation loss of plasmons and the reflectance at resonator edges (for definition, see supplementary materials). In contrast to the indirect coupling to acoustic plasmons, the direct coupling from free-space waves to acoustic plasmons is inefficient due to the larger difference in wavenumber between them as can be seen

in the BP(ribbon)/metal(ribbon) case. In addition to higher extinction intensity, the BP(sheet)/metal(ribbon) resonators are more suitable for practical implementation compared to the other designs since potentially, no patterning steps are required after the deposition of BP, thereby minimizing process-induced damages to BP.

CONCLUSION

In conclusion, we have investigated the anisotropic dispersion for the acoustic plasmons in a freestanding BP layer coupled to a conducting plate. The dispersion for the acoustic plasmons was found to scale linearly with ω in the mid- and far-IR regimes except in the long wavelength limit. At high frequencies, where λ_{ac} becomes comparable to g, it approaches the dispersion of conventional BP plasmons without a conducting plate. Due to larger confinement and narrower plasmon-supporting band, the ZZ case largely deviates from the linear scaling behavior. The analytical results confirmed the numerical results and clearly showed that the linear scaling regime becomes broader for smaller gap size and number of layers, and higher carrier density. Further, we numerically demonstrated different types of acoustic plasmon resonators including BP(ribbon)/metal(ribbon) and BP(sheet)/metal(ribbon) configurations. Among feasible design options, the BP(sheet)/metal(ribbon) resonator exhibited the largest extinction intensity than the other possible configurations considered due to higher coupling efficiency. We developed a modified F-P resonance model to account for the resonant behavior of such a plasmon resonator. Importantly, our new resonator design can be realized using a continuous sheet of BP without nano-patterning, which can introduce defects and edge roughness in BP. While an experimental realization of acoustic plasmon resonances in BP is not trivial, recent advances[47,52] in the growth

of high-quality large-area BP samples show promising routes for the verification of our theoretical predictions. Also, our findings on acoustic plasmons in BP help to develop novel optoelectronic devices using optical anisotropy and extreme field confinement such as metasurfaces,[10,12,13] biosensors,[15,30] optical modulators,[40,41] molecular trapping,[53-55] and photodetectors.[43,44]

METHODS

We used COMSOL Multiphysics with the RF Module for numerical simulations. In order to calculate the dispersion relation for acoustic plasmons in BP along with the reflection phase and amplitude, a port placed inside the simulation domain was used to solve for the eigenmode, launch the mode, and measure the reflection from the terminal interface. Perfectly matched layers (PMLs) were used at all simulation boundaries to increase accuracy. The electric field distributions in Figures 1 and 4 were also calculated in the same configuration. For Figures 5 and 6, we used a plane wave with transverse magnetic polarization to obtain the extinction spectra of two acoustic plasmon resonators. Perfect electrical conductor (PEC) boundary conditions were used at both boundaries to simulate a periodic structure and reduce the computation time through symmetry. In most cases, the conducting plate was assumed to be 50 nm-thick gold with a dielectric function obtained elsewhere.[56] The Drude model is used to approximate the conductivity of multilayer BP (see supplemental material for details). For numerical calculations, BP is modeled as a slab with thickness t and effective permittivity ε_{BP} as defined in the text.[48]

AUTHOR CONTRIBUTIONS.

I.-H.L., L.M.M., and S.-H.O. conceived the idea. I.-H.L. and D.A.M. performed numerical simulations using COMSOL. I.-H.L., L.M.M., K.K., and T.L contributed to theoretical analysis. K.K. and T.L. calculated material parameters. All authors analyzed the data and wrote the paper together.

ACKNOWLEDGMENTS.

This research was supported primarily by the U.S. National Science Foundation (MRSEC Seed grant to I.-H.L., T.L., K.K., S.-H.O.; ECCS 1610333 to S.-H.O.). L.M.-M. acknowledges financial support by the Spanish MINECO under contract No. MAT2014-53432-C5. D.A.M. acknowledges the NIH Biotechnology Training Grant (NIH T32 GM008347). L.M.-M., T.L., and S.-H.O. also thank support from the Institute for Mathematics and its Applications (IMA) at the University of Minnesota.

Notes. The authors declare no competing financial interests.

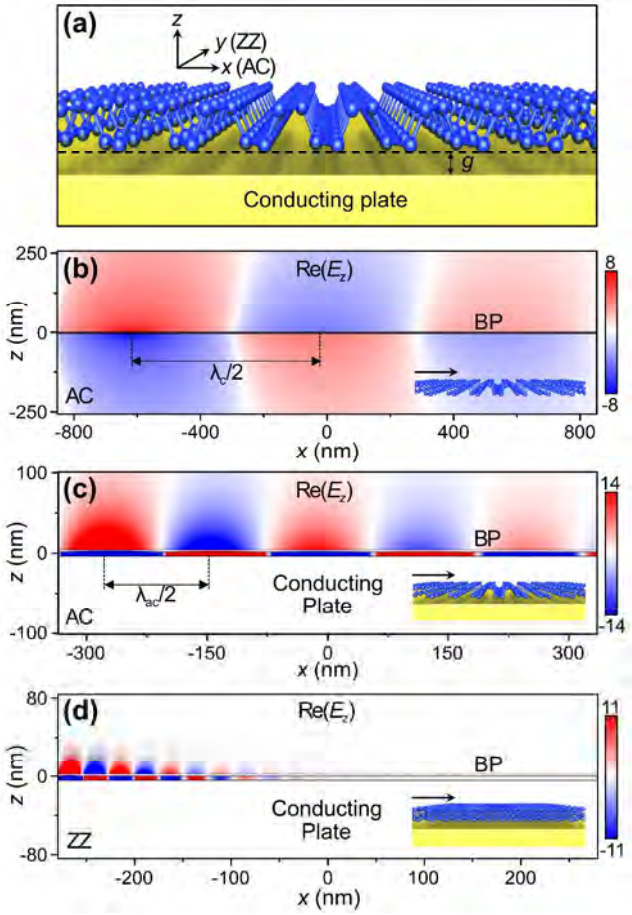

Figure 1. (a) The geometrical configuration supporting acoustic plasmons. The *z*-component of the electric field of (b) conventional plasmons propagating in the AC direction with the plasmon wavelength, λ_c, and acoustic plasmons propagating in (c) the AC and (d) ZZ direction with the plasmon wavelength λ_{ac} are shown for the free-space wavelength of 25 μm. In (c) and (d), the gap between the BP and the conducting plate was 5 nm. The insets in (b)-(d) show the geometrical configurations considered and the arrows represent the propagation direction of plasmons (the positive *x* direction in all cases).

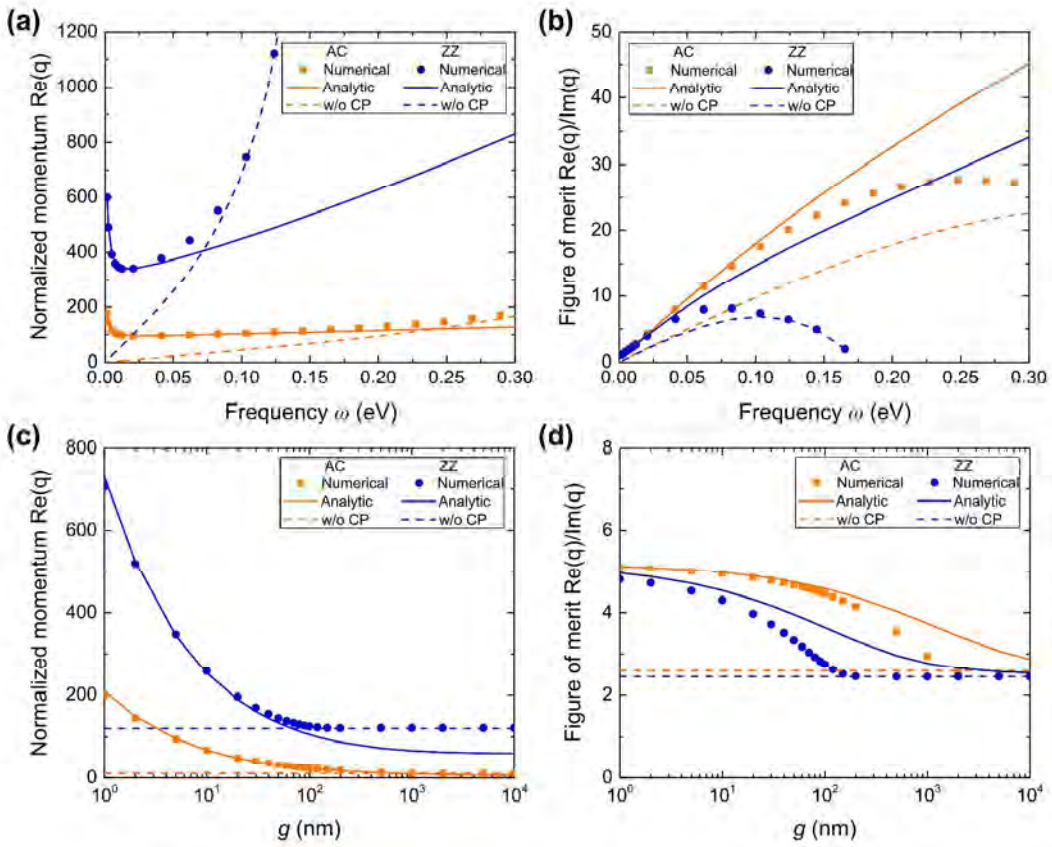

Figure 2. (a) The plasmon dispersion and (b) figure of merit (FOM) along the AC and ZZ directions. Here, we assumed g = 5 nm. (c) The momentum and (d) FOM as a function of g along the AC and ZZ directions. In all cases, the dispersions given in terms of the real part of the dimensionless momentum, $q \equiv k/k_0$ and FOM is defined as Re(q)/Im(q). Numerical and analytical results are plotted together, and the numerical results for plasmons without a conducting plate (CP) are given for comparison.

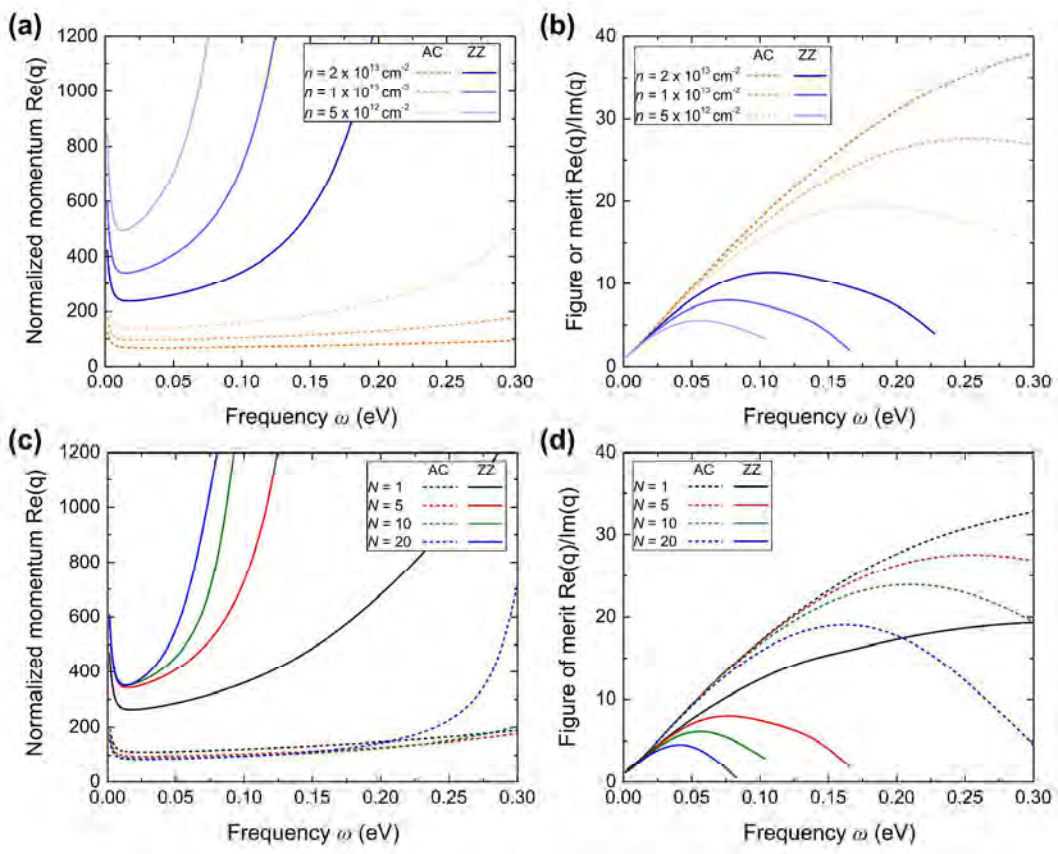

Figure 3. Effect of electron density, *n*, on (a) plasmon dispersion and (b) FOM. *n* is varied from 5×10^{12}, 1×10^{13} to 2×10^{13} cm^{-2}. The effect of the number of layers, *N*, on (c) plasmon dispersion and (d) FOM. Here, 1, 5, 10, and 20 layers are considered.

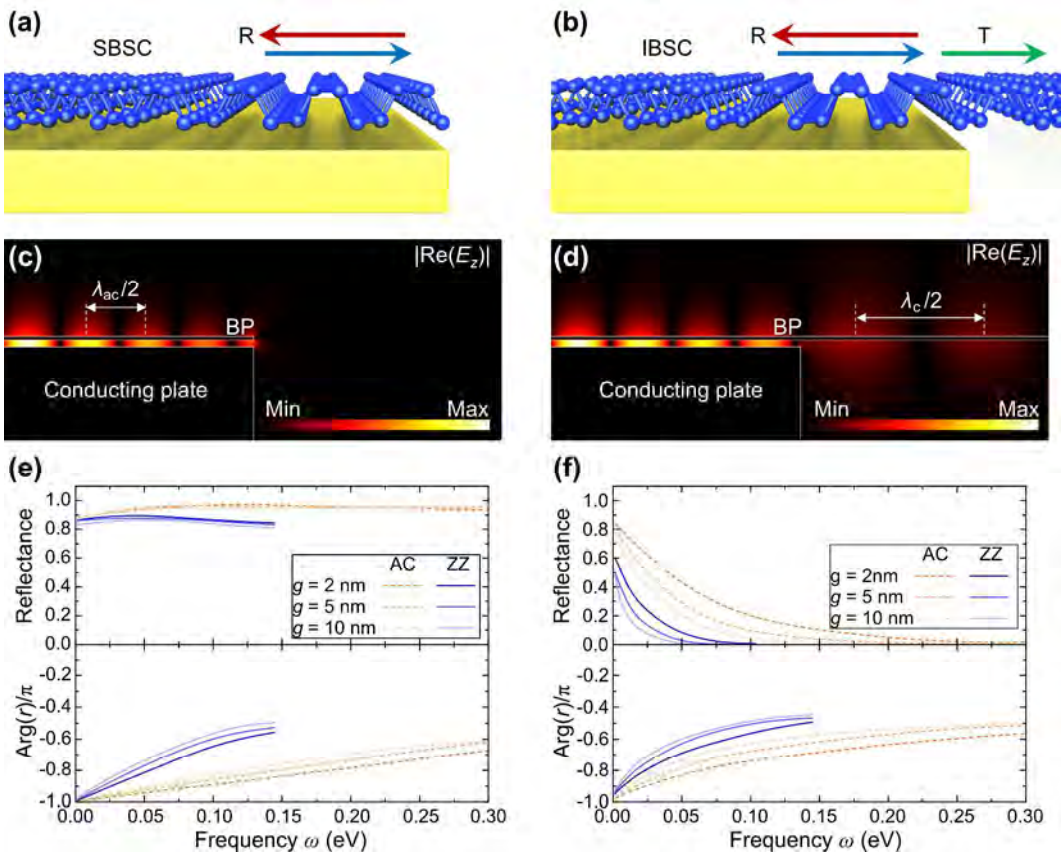

Figure 4. Schematic illustration of reflection at two different types of edge termination with (a) semi-infinite and (b) infinite BP sheet over the edge of a semi-infinite conducting plate (SBSC and IBSC cases, respectively). Electrical field distribution after reflection for (c) SBSC and (d) IBSC cases for AC direction, g = 5 nm, and λ_0 = 25 μm. Reflection amplitude and phase of an acoustic plasmon after reflection at the edge for (e) SBSC and (f) IBSC cases for different g and crystal axes. Here, r denotes the reflection coefficient for acoustic plasmons.

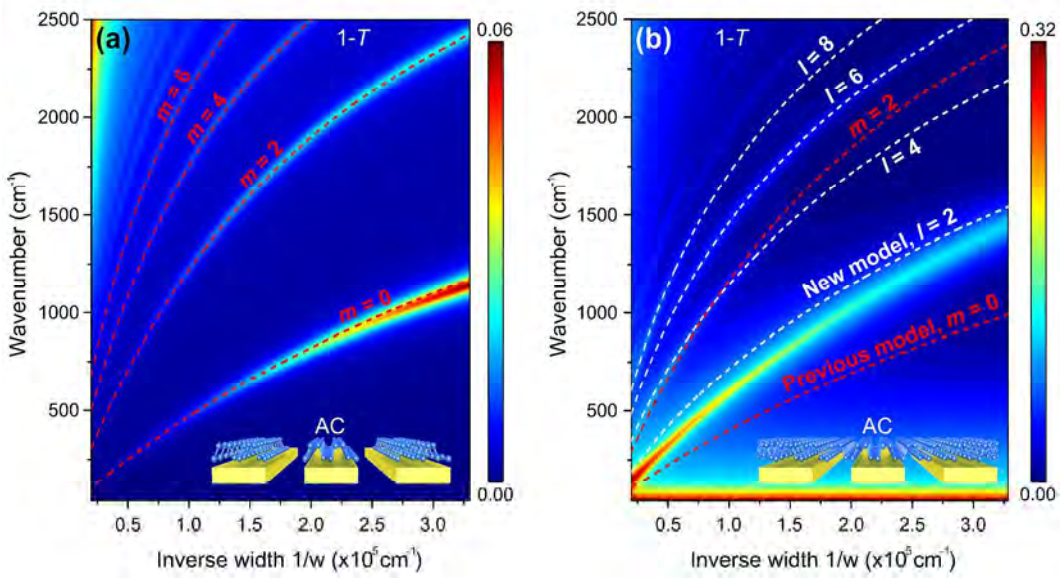

Figure 5. Extinction spectra of BP acoustic plasmon resonators with (a) BP(ribbon)/metal(ribbon) and (b) BP(sheet)/metal(ribbon) for the AC direction as a function of inverse conducting plate width ($1/w$) under illumination by a normally incident plane wave with transverse magnetic polarization. Red dashed lines are the estimated resonant frequencies for different orders of interference (m) using the conventional Fabry-Perot resonance equation. White dashed lines are the estimation from the modified Fabry-Perot resonance equation for different orders (l).

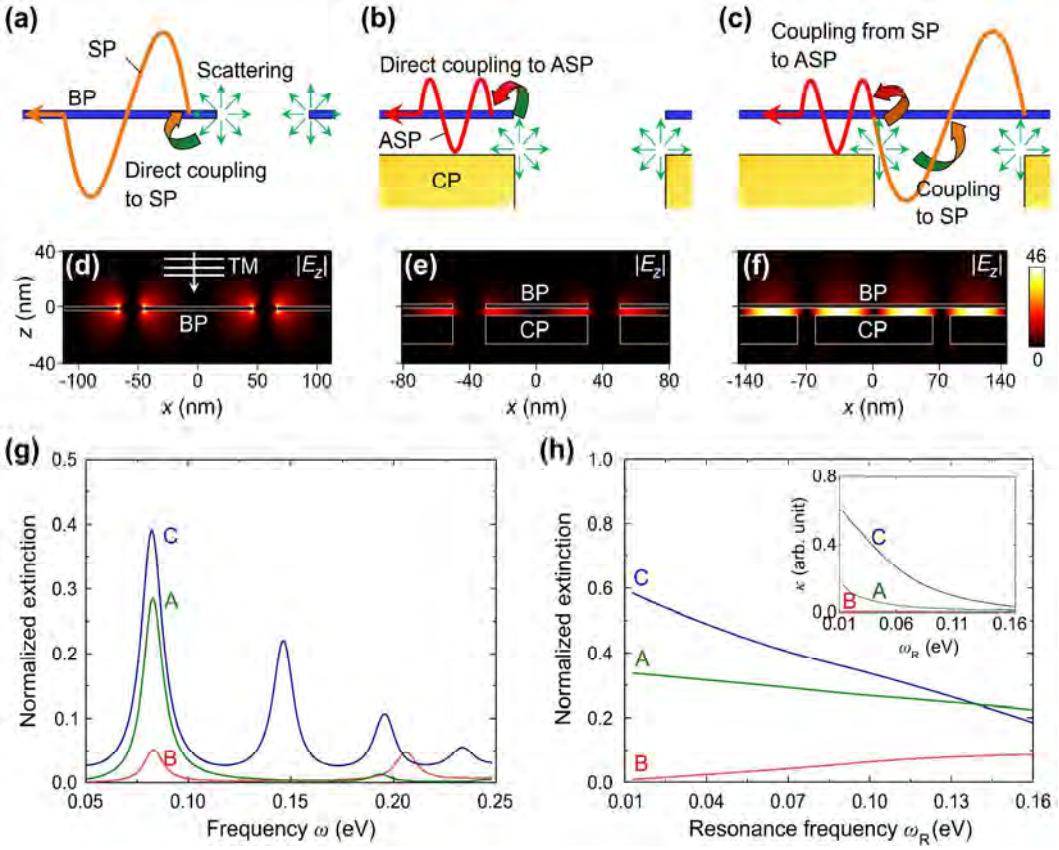

Figure 6. Schematic illustration of coupling routes to surface plasmons (SP) or acoustic surface plasmons (ASP) for (a) BP(ribbon) ('A'), (b) BP(ribbon)/CP(ribbon) ('B'), and (c) BP(sheet)/CP(ribbon) ('C') resonators where 'CP' means a conducting plate. The *z* electric field enhancement on resonance at $\lambda_0 = 15$ μm ($\omega = 0.083$ eV//$\hbar$) for (d) A, (e) B, and (f) C resonators. (g) Extinction spectra for three different geometries where the first-occurring resonance coincide at $\lambda_0 = 15$ μm. In (d)-(g), the widths of a resonator unit were 92, 61, and 128 nm for A, B, and C resonators, respectively. (h) Normalized extinction intensities on resonance as a function of resonance frequency for three different geometries. Inset shows corresponding coupling efficiency κ. In (d)-(h), both the spacing between two resonator units and the thickness of a conducting plate were fixed to be 20 nm for optimized performance. The resonators were illuminated by a normally incident plane wave with transverse magnetic (TM) polarization.

REFERENCES

(1) Novoselov, K.; Jiang, D.; Schedin, F.; Booth, T.; Khotkevich, V.; Morozov, S.; Geim, A. Two-Dimensional Atomic Crystals. *Proc. Natl. Acad. Sci. U.S.A.* **2005,** *102*, 10451-10453.

(2) Avouris, P.; Heinz, T. F.; Low, T. *2D Materials*. Cambridge University Press: **2017**.

(3) Bolotin, K. I.; Sikes, K.; Jiang, Z.; Klima, M.; Fudenberg, G.; Hone, J.; Kim, P.; Stormer, H. Ultrahigh Electron Mobility in Suspended Graphene. *Solid State Commun.* **2008,** *146*, 351-355.

(4) Mayorov, A. S.; Gorbachev, R. V.; Morozov, S. V.; Britnell, L.; Jalil, R.; Ponomarenko, L. A.; Blake, P.; Novoselov, K. S.; Watanabe, K.; Taniguchi, T.; Geim, A. K. Micrometer-Scale Ballistic Transport in Encapsulated Graphene at Room Temperature. *Nano Lett.* **2011,** *11*, 2396-2399.

(5) Zhang, Y.; Tan, Y.-W.; Stormer, H. L.; Kim, P. Experimental Observation of the Quantum Hall Effect and Berry's Phase in Graphene. *Nature* **2005,** *438*, 201-204.

(6) Koppens, F. H. L.; Chang, D. E.; García de Abajo, F. J. Graphene Plasmonics: A Platform for Strong Light–Matter Interactions. *Nano Lett.* **2011,** *11*, 3370-3377.

(7) Britnell, L.; Ribeiro, R.; Eckmann, A.; Jalil, R.; Belle, B.; Mishchenko, A.; Kim, Y.-J.; Gorbachev, R.; Georgiou, T.; Morozov, S.; Grigorenko, A. N.; Geim, A. K.; Casiraghi, C.; Castro Neto, A. H.; Novoselov, K. S. Strong Light-Matter Interactions in Heterostructures of Atomically Thin Films. *Science* **2013,** *340*, 1311-1314.

(8) Sun, Z.; Martinez, A.; Wang, F. Optical Modulators with 2D Layered Materials. *Nat. Photon.* **2016,** *10*, 227-238.

(9) Whitney, W. S.; Sherrott, M. C.; Jariwala, D.; Lin, W.-H.; Bechtel, H. A.; Rossman, G. R.; Atwater, H. A. Field Effect Optoelectronic Modulation of Quantum-Confined Carriers in Black Phosphorus. *Nano Lett.* **2016,** *17*, 78-84.

(10) Fallahi, A.; Perruisseau-Carrier, J. Design of Tunable Biperiodic Graphene Metasurfaces. *Phys. Rev. B* **2012,** *86*, 195408.

(11) Jang, M. S.; Brar, V. W.; Sherrott, M. C.; Lopez, J. J.; Kim, L.; Kim, S.; Choi, M.; Atwater, H. A. Tunable Large Resonant Absorption in a Midinfrared Graphene Salisbury Screen. *Phys. Rev. B* **2014,** *90*, 165409.

(12) Carrasco, E.; Tamagnone, M.; Mosig, J. R.; Low, T.; Perruisseau-Carrier, J. Gate-Controlled Mid-Infrared Light Bending with Aperiodic Graphene Nanoribbons Array. *Nanotechnology* **2015,** *26*, 134002.

(13) Huidobro, P. A.; Kraft, M.; Maier, S. A.; Pendry, J. B. Graphene as a Tunable Anisotropic or Isotropic Plasmonic Metasurface. *ACS Nano* **2016,** *10*, 5499-5506.

(14) Li, Y.; Yan, H.; Farmer, D. B.; Meng, X.; Zhu, W.; Osgood, R. M.; Heinz, T. F.; Avouris, P. Graphene Plasmon Enhanced Vibrational Sensing of Surface-Adsorbed Layers. *Nano Lett.* **2014,** *14*, 1573-1577.

(15) Rodrigo, D.; Limaj, O.; Janner, D.; Etezadi, D.; de Abajo, F. J. G.; Pruneri, V.; Altug, H. Mid-Infrared Plasmonic Biosensing with Graphene. *Science* **2015,** *349*, 165-168.

(16) Fang, Z.; Liu, Z.; Wang, Y.; Ajayan, P. M.; Nordlander, P.; Halas, N. J. Graphene-Antenna Sandwich Photodetector. *Nano Lett.* **2012,** *12*, 3808-3813.

(17) Koppens, F. H. L.; Mueller, T.; Avouris, P.; Ferrari, A.; Vitiello, M.; Polini, M. Photodetectors Based on Graphene, Other Two-Dimensional Materials and Hybrid Systems. *Nat. Nanotechnol.* **2014,** *9*, 780-793.

(18) Hwang, E.; Sarma, S. D. Dielectric Function, Screening, and Plasmons in Two-Dimensional Graphene. *Phys. Rev. B* **2007,** *75*, 205418.

(19) Jablan, M.; Buljan, H.; Soljačić, M. Plasmonics in Graphene at Infrared Frequencies. *Phys. Rev. B* **2009,** *80*, 245435.

(20) Yan, H.; Low, T.; Zhu, W.; Wu, Y.; Freitag, M.; Li, X.; Guinea, F.; Avouris, P.; Xia, F. Damping Pathways of Mid-Infrared Plasmons in Graphene Nanostructures. *Nat. Photon.* **2013,** *7*, 394-399.

(21) Chen, J.; Badioli, M.; Alonso-González, P.; Thongrattanasiri, S.; Huth, F.; Osmond, J.; Spasenović, M.; Centeno, A.; Pesquera, A.; Godignon, P.; Elorza, A. Z.; Camara, N.; Garcia de Abajo, F.; Hillenbrand, R.; Koppens, F. H. L. Optical Nano-Imaging of Gate-Tunable Graphene Plasmons. *Nature* **2012,** *487*, 77-81.

(22) Fei, Z.; Rodin, A.; Andreev, G.; Bao, W.; McLeod, A.; Wagner, M.; Zhang, L.; Zhao, Z.; Thiemens, M.; Dominguez, G.; Fogler, M. M.; Castro Neto, A. H.; Lau, C. N.; Keilmann, F.; Basov, D. N. Gate-Tuning of Graphene Plasmons Revealed by Infrared Nano-Imaging. *Nature* **2012,** *487*, 82-85.

(23) Caldwell, J. D.; Vurgaftman, I.; Tischler, J. G.; Glembocki, O. J.; Owrutsky, J. C.; Reinecke, T. L. Atomic-Scale Photonic Hybrids for Mid-Infrared and Terahertz Nanophotonics. *Nat. Nanotechnol.* **2016,** *11*, 9-15.

(24) Fang, Z.; Wang, Y.; Schlather, A. E.; Liu, Z.; Ajayan, P. M.; García de Abajo, F. J.; Nordlander, P.; Zhu, X.; Halas, N. J. Active Tunable Absorption Enhancement with Graphene Nanodisk Arrays. *Nano Lett.* **2014,** *14*, 299-304.

(25) Bao, Q.; Zhang, H.; Wang, B.; Ni, Z.; Lim, C. H. Y. X.; Wang, Y.; Tang, D. Y.; Loh, K. P. Broadband Graphene Polarizer. *Nat. Photon.* **2011,** *5*, 411-415.

(26) Goossens, S.; Navickaite, G.; Monasterio, C.; Gupta, S.; Piqueras, J. J.; Pérez, R.; Burwell, G.; Nikitskiy, I.; Lasanta, T.; Galán, T.; Puma, E.; Ceneno, A.; Pesquera, A.; Zurutuza, A.; Konstantatos, G.; Koppens, F. H. L. Broadband Image Sensor Array Based on Graphene–CMOS Integration. *Nat. Photon.* **2017,** *11*, 366-371.

(27) Pisarra, M.; Sindona, A.; Riccardi, P.; Silkin, V.; Pitarke, J. Acoustic Plasmons in Extrinsic Free-Standing Graphene. *New J. Phys.* **2014,** *16*, 083003.

(28) Alonso-González, P.; Nikitin, A. Y.; Gao, Y.; Woessner, A.; Lundeberg, M. B.; Principi, A.; Forcellini, N.; Yan, W.; Vélez, S.; Huber, A. J.; Watanabe, K.; Taniguchi, T.; Casanova, F.; Hueso, L,; Polini, M.; Hone, J.; Koppens, F. H. L.; Hillenbrand, R. Acoustic Terahertz Graphene Plasmons Revealed by Photocurrent Nanoscopy. *Nat. Nanotechnol.* **2017,** *12*, 31-35.

(29) Lundeberg, M. B.; Gao, Y.; Asgari, R.; Tan, C.; Van Duppen, B.; Autore, M.; Alonso-González, P.; Woessner, A.; Watanabe, K.; Taniguchi, T.; Hillenbrand, R.; Hone, J.; Polini, M.; Koppens, F. H. L. Tuning Quantum Nonlocal Effects in Graphene Plasmonics. *Science* **2017,** 357, 187-191.

(30) Chen, S.; Autore, M.; Li, J.; Li, P.; Alonso-Gonzalez, P.; Yang, Z.; Martin-Moreno, L.; Hillenbrand, R.; Nikitin, A. Y. Acoustic Graphene Plasmon Nanoresonators for Field-Enhanced Infrared Molecular Spectroscopy. *ACS Photonics* **2017,** *4*, 3089-3097.

(31) Hwang, E.; Sarma, S. D. Plasmon Modes of Spatially Separated Double-Layer Graphene. *Phys. Rev. B* **2009,** *80*, 205405.

(32) Stauber, T.; Gómez-Santos, G. Plasmons in Layered Structures Including Graphene. *New J. Phys.* **2012,** *14*, 105018.

(33) Rodrigo, D.; Tittl, A.; Limaj, O.; de Abajo, F. J. G.; Pruneri, V.; Altug, H. Double-Layer Graphene for Enhanced Tunable Infrared Plasmonics. *Light Sci. Appl.* **2017,** *6*, e16277.

(34) Low, T.; Roldán, R.; Wang, H.; Xia, F.; Avouris, P.; Moreno, L. M.; Guinea, F. Plasmons and Screening in Monolayer and Multilayer Black Phosphorus. *Phys. Rev. Lett.* **2014,** *113*, 106802.

(35) Liu, H.; Neal, A. T.; Zhu, Z.; Luo, Z.; Xu, X.; Tománek, D.; Peide, D. Y. Phosphorene: An Unexplored 2D Semiconductor with a High Hole Mobility. *ACS Nano* **2014,** *8*, 4033-4041.

(36) Li, L.; Yu, Y.; Ye, G. J.; Ge, Q.; Ou, X.; Wu, H.; Feng, D.; Chen, X. H.; Zhang, Y. Black Phosphorus Field-Effect Transistors. *Nat. Nanotechnol.* **2014,** *9*, 372-377.

(37) Liu, Z.; Aydin, K. Localized Surface Plasmons in Nanostructured Monolayer Black Phosphorus. *Nano Lett.* **2016,** *16*, 3457-3462.

(38) Huber, M. A.; Mooshammer, F.; Plankl, M.; Viti, L.; Sandner, F.; Kastner, L. Z.; Frank, T.; Fabian, J.; Vitiello, M. S.; Cocker, T. L.; Huber, R. Femtosecond Photo-Switching of Interface Polaritons in Black Phosphorus Heterostructures. *Nat. Nanotechnol.* **2017,** *12*, 207-211..

(39) Low, T.; Chaves, A.; Caldwell, J. D.; Kumar, A.; Fang, N. X.; Avouris, P.; Heinz, T. F.; Guinea, F.; Martin-Moreno, L.; Koppens, F. H. L. Polaritons in Layered Two-Dimensional Materials. *Nat. Mater.* **2017,** *16*, 182-194.

(40) Zhang, R.; Zhang, Y.; Yu, H.; Zhang, H.; Yang, R.; Yang, B.; Liu, Z.; Wang, J. Broadband Black Phosphorus Optical Modulator in the Spectral Range from Visible to Mid□Infrared. *Adv. Opt. Mater.* **2015,** *3*, 1787-1792.

(41) Peng, R.; Khaliji, K.; Youngblood, N.; Grassi, R.; Low, T.; Li, M. Midinfrared Electro-Optic Modulation in Few-Layer Black Phosphorus. *Nano Lett.* **2017,** *17*, 6315-6320.

(42) Khaliji, K.; Fallahi, A.; Martin-Moreno, L.; Low, T. Tunable Plasmon-Enhanced Birefringence in Ribbon Array of Anisotropic Two-Dimensional Materials. *Phys. Rev. B* **2017,** *95*, 201401.

(43) Engel, M.; Steiner, M.; Avouris, P. Black Phosphorus Photodetector for Multispectral, High-Resolution Imaging. *Nano Lett.* **2014,** 14, 6414-6417.

(44) Youngblood, N.; Chen, C.; Koester, S. J.; Li, M. Waveguide-Integrated Black Phosphorus Photodetector with High Responsivity and Low Dark Current. *Nat. Photon.* **2015,** *9*, 247-252.

(45) Perello, D. J.; Chae, S. H.; Song, S.; Lee, Y. H. High-Performance N-Type Black Phosphorus Transistors with Type Control via Thickness and Contact-Metal Engineering. *Nat. Commun.* **2015,** *6*, 7809.

(46) Liu, H.; Du, Y.; Deng, Y.; Peide, D. Y. Semiconducting Black Phosphorus: Synthesis, Transport Properties and Electronic Applications. *Chem. Soc. Rev.* **2015,** *44*, 2732-2743.

(47) Yasaei, P.; Kumar, B.; Foroozan, T.; Wang, C.; Asadi, M.; Tuschel, D.; Indacochea, J. E.; Klie, R. F.; Salehi□Khojin, A. High□Quality Black Phosphorus Atomic Layers by Liquid□Phase Exfoliation. *Adv. Mater.* **2015,** *27*, 1887-1892.

(48) Vakil, A.; Engheta, N. Transformation Optics Using Graphene. *Science* **2011,** *332*, 1291-1294.

(49) Nikitin, A. Y.; Low, T.; Martin-Moreno, L. Anomalous Reflection Phase of Graphene Plasmons and Its Influence on Resonators. *Phys. Rev. B* **2014,** *90*, 041407.

(50) De Waele, R.; Burgos, S. P.; Polman, A.; Atwater, H. A. Plasmon Dispersion in Coaxial Waveguides from Single-Cavity Optical Transmission Measurements. *Nano Lett.* **2009,** *9*, 2832-2837.

(51) Yoo, D.; Nguyen, N.-C.; Martin-Moreno, L.; Mohr, D. A.; Carretero-Palacios, S.; Shaver, J.; Peraire, J.; Ebbesen, T. W.; Oh, S.-H. High-Throughput Fabrication of Resonant Metamaterials with Ultrasmall Coaxial Apertures via Atomic Layer Lithography. *Nano Lett.* **2016,** *16*, 2040-2046.

(52) Zhang, G.; Huang, S.; Chaves, A.; Song, C.; Özçelik, V. O.; Low, T.; Yan, H. Infrared Fingerprints of Few-Layer Black Phosphorus. *Nat. Commun.* **2017,** *8*, 14071.

(53) Juan, M. L.; Righini, M.; Quidant, R. Plasmon Nano-Optical Tweezers. *Nat. Photon.* **2011,** *5*, 349-356.

(54) Zhang, J.; Liu, W.; Zhu, Z.; Yuan, X.; Qin, S. Towards Nano-Optical Tweezers with Graphene Plasmons: Numerical Investigation of Trapping 10-nm Particles with Mid-Infrared Light. *Sci. Rep.* **2016,** *6*, 38086.

(55) Barik, A.; Zhang, Y.; Grassi, R.; Nadappuram, B. P.; Edel, J. B.; Low, T.; Koester, S. J.; Oh, S.-H. Graphene-Edge Dielectrophoretic Tweezers for Trapping of Biomolecules. *Nat. Commun.* **2017,** *8*, 1867.

(56) Ordal, M. A.; Bell, R. J.; Alexander, R. W.; Long, L. L.; Querry, M. R. Optical Properties of Au, Ni, and Pb at Submillimeter Wavelengths. *Appl. Opt.* **1987,** *26*, 744-752.

For Table of Contents Use Only

Anisotropic Acoustic Plasmons in Black Phosphorus

In-Ho Lee, Luis Martin-Moreno, Daniel A. Mohr, Kaveh Khaliji, Tony Low, and Sang-Hyun Oh